Robotic Underwater Propulsion Inspired by the Octopus Multi-arm Swimming

Michael Sfakiotakis, Asimina Kazakidi, Nikolaos Pateromichelakis,
John A. Ekaterinaris and Dimitris P. Tsakiris

***Abstract*— The multi-arm morphology of octopus-inspired robotic systems may allow their aquatic propulsion, in addition to providing manipulation functionalities, and enable the development of flexible robotic tools for underwater applications. In the present paper, we consider the multi-arm swimming behavior of the octopus, which is different than their, more usual, jetting behavior, and is often used to achieve higher propulsive speeds, e.g., for chasing prey. We develop a multi-arm segmented dynamical model of such robotic systems, to study the generation of this mode of propulsion. The model includes fluid drag contributions, which we support by detailed computational fluid dynamic analysis. The parametric study of the kinematic parameters of the system, during sculling motions of the arms, indicated the arm oscillation characteristics that optimize the generation of propulsive forces. Similar studies are performed for undulatory arm motions. Experiments with a robotic prototype in a water tank support these simulation results.**

***Index Terms*— Biologically-Inspired Robots, Underwater Propulsion, Hydrodynamics, Octopus.**

I. INTRODUCTION

Underwater robots are becoming increasingly important in industrial and service applications, such as search-and-rescue operations in narrow flooded zones or undersea shipwrecks, industrial inspection or maintenance in tortuous fluid-filled spaces, as well as shallow- or deep-water marine exploration. The scope of such applications can be significantly enhanced by equipping these underwater vehicles, which frequently employ propellers for propulsion, with robotic manipulators, endowed with multi-function capabilities. The possibility of using these manipulators also for propulsion has not been examined in detail, and could be of some interest.

Indeed, marine animals like the octopus, may use their agile arms in various locomotion modes, like crawling or walking on the seabed or for complementing their frequently-employed jet propulsion. Lacking skeletal support, the octopus arms are highly dexterous and can achieve complex shapes and perform movements, such as reaching and fetching, by activating several distinct groups of arm muscles [1], [2]. In a behavior known as *medusoid jetting*, octopuses open and close their arms and arm crown in synchrony, like an umbrella, to produce bursts of activity, supplementing jet propulsion. The *abdopus aculeatus* occasionally use this mode of locomotion in the wild, during sustained jetting, to chase conspecifics (Fig. 1) or prey [1]. The kinematics of arm swimming do not appear to have been investigated in detail, although two essential features could be extracted from related data: each stroke is composed of two phases, one where the arms, initially trailing behind, open by bending outwards relatively slowly, and one where they return fast to their initial position.

Investigations are currently under way to develop dexterous robotic manipulator arms inspired by the morphology and mechanical properties of the octopus arms [3]–[5]. However, the present study focuses on employing a set of such robotic arms for aquatic propulsion, not for manipulation. As all arms of the octopus appear to move in a similar, and synchronized, manner during medusoid jetting, we, initially, consider a planar version of this behavior, that

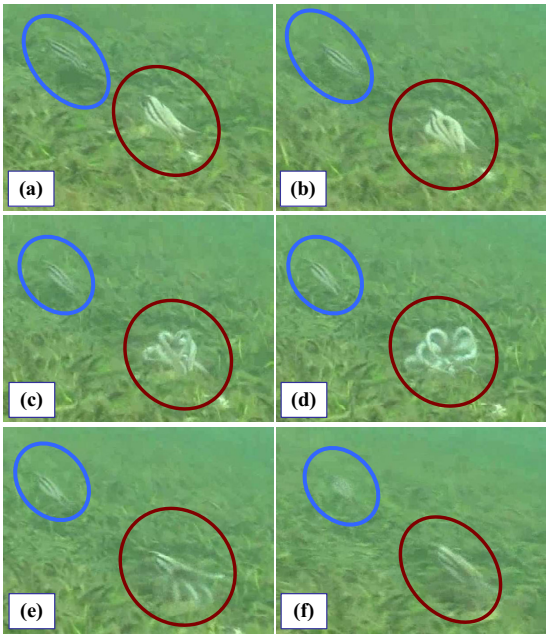

Fig. 1. Medusoid jetting by two *Abdopus aculeatus* in the wild [1]. Animals are encircled for clarity. (a)-(d) Slow recovery stroke, (d)-(f) Fast power stroke, (h) Coasting (time between frames is constant).

This work was supported by the European Commission via the ICT-FET OCTOPUS Integrated Project, under contract No. 231608.

M. Sfakiotakis, A. Kazakidi, N. Pateromichelakis and D.P. Tsakiris are with the Institute of Computer Science, Foundation for Research and Technology – Hellas (FORTH), N. Plastira 100, Vassilika Vouton, GR-70013, Heraklion, Greece. M. Sfakiotakis is also with the Dept. of Electrical Engineering, Technological Educational Institute of Crete, Heraklion, Greece. {sfakios, kazakidi, nikospat, tsakiris}@ics.forth.gr. J.A. Ekaterinaris is with the Institute of Applied & Computational Mathematics, FORTH, GR 70013, Heraklion, Greece and with the School of Mechanical and Aerospace Engineering, University of Patras, GR 26500 Patra, Greece. Email: ekaterin@iacm.forth.gr

Preprint submitted to 2012 IEEE International Conference on Robotics and Automation. Received September 16, 2011.

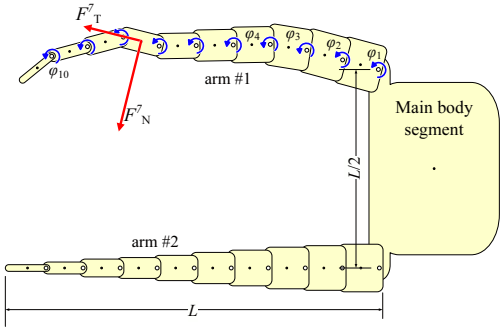

Fig. 2. Configuration of the two-arm swimming mechanism

involves only two arms flapping in their aquatic environment. Towards this end, computational models have been developed to study propulsion generation for a robotic system featuring a pair of multi-segment arm-like appendages. A fluid drag model, commonly employed in the robotic literature, models the interaction of the arms' segments with the aquatic environment. Detailed computational fluid dynamics (CFD) analysis of robotic arms, which realistically mimick the morphology of octopus arms, has been used to validate this force model, and to calculate the values for the fluid force coefficients involved in it. Simulation results, implementing various motion control schemes for the arms, demonstrate the generation of propulsive forces by sculling and undulatory movements of the arms. These computational studies are supported by preliminary experimental results of a two-arm robotic prototype in a water tank.

Section II of the paper presents the computational model developed to simulate the investigated swimming mechanisms, while Section III describes the fluid dynamics model of the octopus arm. The analysis of the CFD results, and the way these have been related to the model of the robotic system is provided in Section IV. A series of simulations of the swimming mechanism, which include a parametric study of the effect of the various kinematic parameters on propulsive speed is described in Section V. Finally, Section VI describes the experimental testbed and presents the obtained results.

II. MODEL OF THE SWIMMING MECHANISM

A. Mechanical model

As a first approximation towards the development of octopus-inspired aquatic propulsion strategies, the mechanism shown in Fig. 2 is considered, comprising a pair of arm-like appendages, attached to the rear side of a main body segment. Each arm is modelled as a kinematic chain of $n = 10$ cylinder-shaped rigid segments, interconnected by 1-dof planar rotary joints. The inertial and geometric properties of these segments have been appropriately selected to correspond to the segmentation of the continuous arm considered in the fluid dynamics analysis of Section III The computational model of the arm dynamics has been implemented in the SIMUUN simulation environment, which is based on the SimMechanics toolbox of Simulink. Using this framework, internal changes in the shape of the arm are imposed by explicitly prescribing angular trajectories for the mechanism's rotary joints φ_i ($i = 1..n$), while the interaction with the aquatic environment is described using a simple fluid drag model (see below). Note that the arm is assumed to be neutrally buoyant, hence facilitating this preliminary study by allowing us to neglect gravitational and buoyancy forces. Finally, the presence of two arms in the system (their anchor points to the main body are distanced by $L/2$) increases the overall propulsion speed and, more importantly, allows for effective cancellation of undesirable yawing motions.

B. Fluid drag model

The fluid drag model, used in SIMUUN to simulate the interaction of the arm segments with the aquatic environment, is a first approximation of the hydrodynamics involved, assuming that: (i) fluid forces are mainly inertial (roughly for a Reynolds number $400 < Re < 4 \cdot 10^5$), (ii) the fluid is stationary, so that its force on a single segment is due only to the motion of that segment, and (iii) the tangential (F_T) and normal (F_N) components of the fluid force are decoupled. These are then calculated, for individual segments as:

$$\begin{aligned} F_T^i &= -\lambda_T^i \operatorname{sgn}(v_T^i) \cdot (v_T^i)^2 \\ \text{and} \quad F_N^i &= -\lambda_N^i \operatorname{sgn}(v_N^i) \cdot \left(v_N^i\right)^2 \end{aligned} \tag{1}$$

where v_T^i and v_N^i are the tangential and normal components of the velocity of the ith segment, while λ_T^i and λ_N^i denote the segment's drag coefficients associated with each force component. The use of such a resistive fluid force model dates back to the study of the undulatory swimming of elongate animals in [6], and has since been widely adopted in the analysis of similarly-shaped bio-inspired robotic underwater systems (see, e.g., [7]–[10]). It should also be pointed out that the computational fluid dynamics (CFD) investigations, presented in Sections III and IV, provide further evidence for the validity of adopting this approach, at least for the type of arm movements considered in the present study, and are

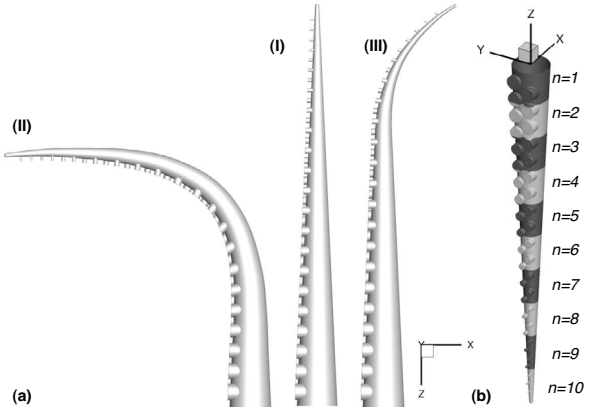

Fig. 3. (a) Octopus arm models used for computational fluid dynamic analysis: (I) straight, (II) fully bent (concave), and (III) partially bent (convex) arm configurations. (b) Location and numbering of 10 segments on the straight arm.

Preprint submitted to 2012 IEEE International Conference on Robotics and Automation. Received September 16, 2011.

also used to provide estimates for the fluid drag coefficients λ_T^i and λ_N^i in (1).

III. FLUID DYNAMICS (CFD) MODEL

We utilized computational fluid dynamic techniques to evaluate the hydrodynamic forces acting by the fluid on an octopus arm with suckers, in the three-dimensional space.

For that, we considered three octopus arm geometries: a straight arm (Fig. 3a-I), an arm with almost ninety degrees bend (concave configuration, Fig. 3a-II), and an arm with a partial bend at the tip (convex configuration, Fig. 3a-III). The straight arm was approximated as a frustum with a base diameter of D, tip diameter of $0.1D$ and length of $10D$; the relative ratios being within the physiological scales of real octopus arm sizes [11], [12]. The arms included 19 pairs of cylindrical suckers in a staggered pattern [13]. The bent arms were constructed with the use of a morphing technique available in ANSA software package (BETA CAE Systems S.A.). A prismatic element boundary-layer mesh was used at the near wall of the octopus arms, to enable accurate representation of the viscous flow effects. The computational domain was $46D$ long in the axial (x) direction, $31D$ wide in the crossflow (y) direction and $20D$ high in the z direction. The upstream and lateral lips of the arms base were located $15D$ away from the upstream and lateral edges of the domain, respectively. In all cases, the walls of the arms were assumed to be rigid.

The incompressible Navier-Stokes equations were used [14], [15] and water was considered as Newtonian fluid (that is, its viscosity was assumed to be constant)

$$\rho\frac{\partial \mathbf{u}}{\partial t} + \rho(\mathbf{u}\cdot\nabla)\mathbf{u} = -\nabla \mathbf{p} + \mu\nabla^{\mathbf{2}}\mathbf{u}, \qquad \nabla\cdot\mathbf{u} = \mathbf{0} \qquad (2)$$

where $\mathbf{u}$=$[u, v, w]$ is the velocity vector, ρ is the fluid density, p is the pressure, and μ is the dynamic viscosity. The flow is characterized by the Reynolds number, Re_D, a non-dimensional parameter, defined as $Re_D = \rho U D/\mu$, where U is the free stream speed of the fluid and D is the base diameter of the octopus arm. The Reynolds number is a measure of the ratio of inertial forces (ρU^2) to viscous forces ($\mu U/D$). At high Reynolds numbers, inertial forces are dominant, whereas viscous forces become significant only at low Reynolds values. For octopus arms performing reaching movements in seawater, the Reynolds number is of the order of 1000 [16], [11], and therefore, inertial forces prevail ($Re_D >> 1$).

The numerical solution was obtained using Fluent (ANSYS, Canonsburg, PA), where a finite-volume method is applied to solve the governing equations (2), on a moving mesh.

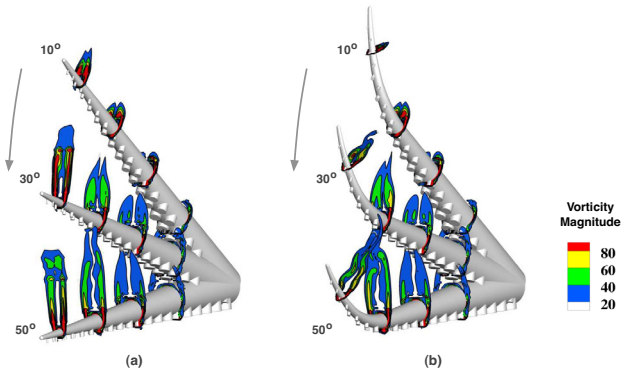

Fig. 4. Superimposed instances of the 3-d flow development around (a) the straight and (b) the bent arms rotating at 1 rad/s, provided by the CFD analysis.

IV. ANALYSIS OF THE CFD RESULTS

A. Straight rotating arm

Initially, we examined the hydrodynamic forces generated on a straight arm with suckers (Fig. 3a-I), rotating impulsively with the suckers-face leading, at a constant speed of $1\ \mathrm{rad}/\mathrm{s}$, which is within the physiological scales for the octopus [17], for a $90°$ rotation (Fig. 4a). The arm was partitioned into ten equal-height segments, as shown in Fig 3b, and the forces were evaluated for each segment. The normal and tangential force components, shown in Fig. 5, can be seen to differ significantly for each segment along the arm and reach a maximum at a distance approximately one third away from the arm tip.

Apart from the observation that both components are, to a large extent, independent of the arm's angular position, it is worth pointing out that these results also indicate the generation of tangential forces by a rotational movement, which, for the straight arm configuration, entails only normal-wise segment velocities. Although this highlights the simplifications in the assumption of decoupled force components involved in the fluid drag model of (1), such an assumption appears to be a fairly reasonable first approximation, as the tangential forces are of a considerably lower amplitude than the normal ones (the normal force is approximately 9 times larger than the tangential force at the position of maximum values). However, it is pointed out that the presence of these tangential forces was taken into consideration for the calculation of the segments' tangential force coefficients for the data presented in Section IV-B below. Note that data from an earlier fluid analysis [13], involving a stationary straight arm at a $0°$ flow incidence angle (i.e., a case where the relative velocity between the arm's segments and the fluid has only a tangential component), showed that only negligible forces were generated in the normal direction, indicating an even weaker coupling between tangential-wise velocities and normal forces.

Focusing on the normal force components, Fig. 6 shows a plot of the ratio between the normal force component F_N^i and $\left(v_N^i\right)^2$, where $v_N^i = \omega z_c^i$ represents the normal velocity of the ith segment's center (z_c^i is the distance of the segment from the center of rotation, i.e., the base of the arm). These data exhibit, for each segment, very little variance with the rotation angle of the arm, so that averaging yields a curve (indicated by the thick dashed line in Fig. 6), well representative of the normal force coefficients λ_N^i, for the case of the straight arm rotating at $\omega = 1\ \mathrm{rad}/\mathrm{s}$.

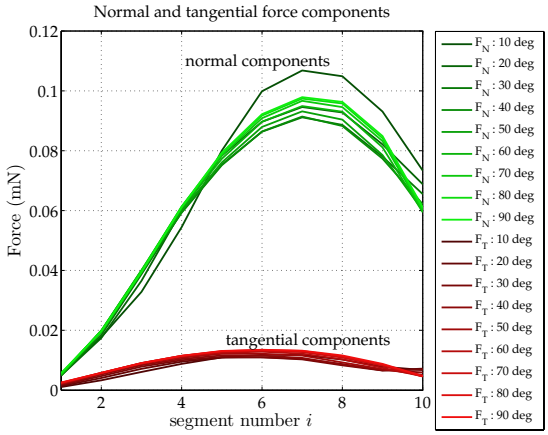

Fig. 5. Normal, F_N^i, and tangential, F_T^i, force components per arm segment, generated by the fluid on an impulsively rotating straight octopus arm with a speed of 1 rad/s.

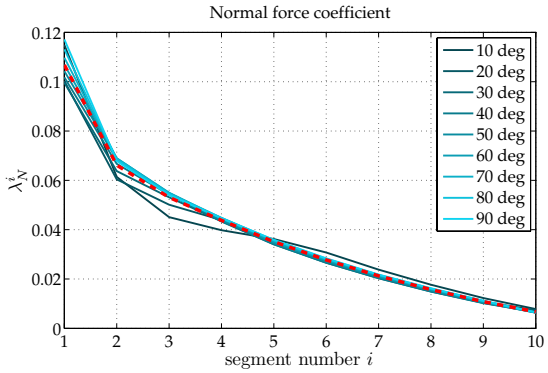

Fig. 6. Normal force coefficients, $\lambda_N^i = F_N^i / \left(v_N^i\right)^2$, per arm segment and per angle, for an impulsively rotating straight octopus arm with 1 rad/s.

B. Bent rotating arms

The above methodology was also employed to analyze CFD data from the partially bent arm (convex configuration, Fig. 3a-III) rotating at $1\ \mathrm{rad/s}$ (Fig. 4b) and at $2\ \mathrm{rad/s}$, as well as for the fully-bent arm (concave configuration, Fig. 3a-II) rotating at $1\ \mathrm{rad/s}$. The arms were partitioned into ten segments in a similar fashion as for the straight arm, although, due to the curvature and the tapering of the arm, the segments had only an approximately equivalent surface area with the straight arm segments.

Much like for the straight arm, the normal forces were found to be largely independent of the arm's rotation angle, permitting the calculation, for each configuration, of an average representative of the normal force coefficient for each of the arm's segments. Fig. 7 shows the results from all four cases, by plotting the normalized force coefficient $\tilde{\lambda}_N^i = \lambda_N^i / c_i$, where $c_i = (l_i D)/(d_i L)$ is a factor describing the inverse aspect ratio of each segment (segment length l_i over the segment's center diameter d_i) relative to the inverse aspect ratio of the whole arm (overall length L over base diameter D). Such a normalization was necessary, in order to account for the slight differences in the dimensions of the arms and the corresponding segments between the three configurations. The results of Fig. 7 indicate that an average could be extracted for the normalized normal force coefficient independently of the exact arm configuration.

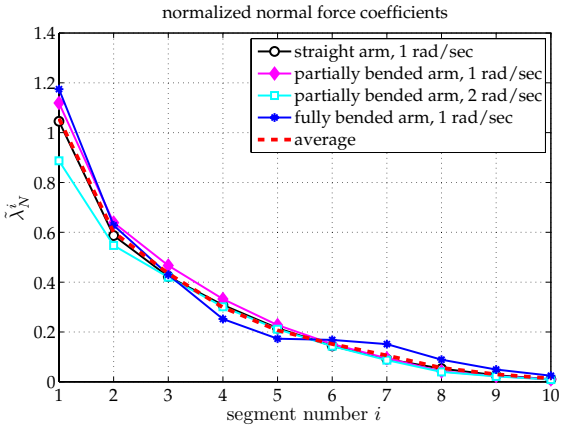

Fig. 7. Normalized normal force coefficients, $\tilde{\lambda}_N^i = \lambda_N^i / c_i$, per arm segment, for a straight (○), a fully bent concave (●), and a partially bent convex (♦) arm configuration, rotating impulsively at 1 rad/s, as well as for a partially bent convex arm (□), rotating at 2 rad/s.

Estimates for the tangential force coefficients were then obtained from the analysis of the CFD data of the two bent arm configurations, based on the fact that their rotational movement involves a tangential, as well as a normal, velocity component for the segments near the arm's tip (specifically, for segments 8-10 of the partially-bent configuration, and for the segments 6-10 of the fully-bent configuration). In order to account for the contribution of the normal velocity components to the tangential forces, the tangential forces from the analysis of the straight arm rotation (c.f. Section IV-A) were first substracted, taking also into account the curvature of the arm, from the tangential forces of these configurations. The thus corrected F_T^i values were then divided by $\left(v_T^i\right)^2$, where v_T^i denotes the tangential velocity of the two configurations' segments near the tip, to obtain the respective λ_T^i values for each case.

The results, in terms of the normalized tangential force coefficient $\tilde{\lambda}_T^i = \lambda_T^i / c_i$, are presented in Fig. 8 and can be used to calculate the final averaged values for segments 6-10. For segments 1-5, the tangential coefficients were extrapolated from the average normalized normal force coefficients $\tilde{\lambda}_N^i$ (as these were estimated by the results of Fig. 7), dividing them by a factor of 3.2. This factor resulted from dividing the above average $\tilde{\lambda}_N^i$ values with the $\tilde{\lambda}_T^i$ ($i = 6..10$) for the fully bent arm (Fig. 8).

V. SIMUUN SIMULATION RESULTS

In the present Section, a series of multi-arm propulsion modes, proposed as a first approximation to capture the main aspects of the octopus' multi-arm swimming, are studied by SIMUUN simulations. We initially develop a simple *sculling* mode, where propulsion is obtained by two-stroke motions of the arms oscillating while held straight, and then proceed to combine these sculling movements with the propagation of a travelling wave along the arms. Simulations employ

Preprint submitted to 2012 IEEE International Conference on Robotics and Automation. Received September 16, 2011.

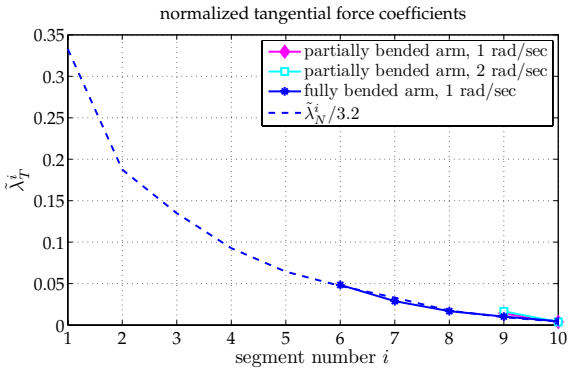

Fig. 8. Normalized tangential force coefficients, $\tilde{\lambda}^i_T = \lambda^i_T/c_i$, per arm segment, for a fully bent concave (●), and a partially bent convex (⧫) arm configuration, rotating impulsively at 1 rad/s, as well as for a partially bent convex arm (□), rotating at 2 rad/s. Dotted line indicates extrapolated data for the other segments.

the mechanical model of the two-arm swimming mechanism described in Section II, using the analysis of the CFD results, presented above, to specify the values for the fluid drag coefficients associated with the arms' segments. In addition, the values of $\lambda_N = \lambda_T = 0.19$ have been selected for the drag coefficients associated with the main body segment of the mechanism (it is noted that the choice of these coefficients was found to have only a limited effect on the qualitative findings of the study presented here).

A. Sculling Mode

In the proposed sculling mode, each arm oscillates as a single straight unit, by setting $\varphi_i = 0$ for the inter-segment joints ($i = 2..n$), while prescribing the following periodic trajectory for the joint connecting the arm to the main body (note that $\varphi_1 = 0$ corresponds to the arm being in its axially oriented position)

$$\varphi_1(t) = \begin{cases} (\psi - A) + 2A\dfrac{t}{(T_s/7)}, & 0 \le t < T_s/7 \\ (\psi + A) - 2A\dfrac{(t - T_s/7)}{(6T_s/7)}, & T_s/7 \le t < T_s \end{cases} \quad (3)$$

Equation (3) describes a two-stroke motion of an angular span $\pm A$ around the angular offset ψ. The velocity ratio between the fast part (power stroke) and the slow part (recovery stroke) of the arm's reciprocating motion has been set to $6:1$. Assuming a prescribed value ω for the angular velocity of the recovery stroke, the period of the overall movement may then be calculated as $T_s = 7A/(3\omega)$. Note that, in order to optimally coordinate the movement of the two arms for thrust generation and cancellation of unwanted yawing movements, the two arms are configured to perform the above motions in a synchronized counter-rotating manner, i.e., both of them moving outwards during the recovery stroke and inwards during the power stroke.

Indicative simulation results, demonstrating propulsion of the system by the sculling mode, are shown in Fig. 9. The 6 snapshots of the system's trajectory, shown in Fig. 9a correspond to the power (upper row) and recovery (lower row) strokes of a single sculling cycle, during which the system moves in the axial "forward" direction. The instantaneous axial velocity $v_b(t)$ of the main body (Fig. 9b), displays a periodic variance of considerable amplitude, in accordance with the arms' sculling movements, and has a positive (i.e. in the "forward" direction) non-zero average value in the steady-state (denoted in the plot by the dashed red line). As expected, the system decelerates during the recovery stroke of the arms, although, for the parameters used in this simulation run, the velocity remains positive throughout. It is also noted that the synchronized motion of the two arms results in the cancellation of unwanted forces, and the system is propelled along a straight trajectory.

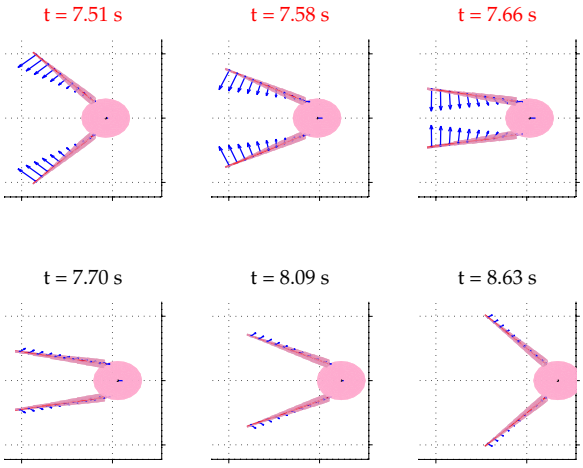

(a) Sculling mode propulsion

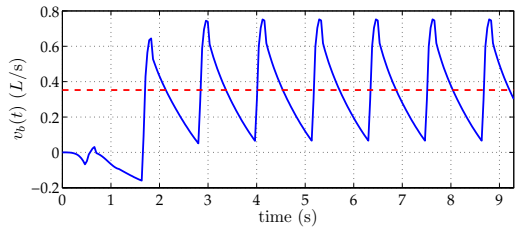

(b) Instantaneous axial velocities of the main body

Fig. 9. Sculling mode simulation results, obtained with $A = 20°$, $\psi = 30°$, and $\omega = 40°/\text{s}$. (a) Visualization of the mechanism for one period of sculling, where the blue arrows denote the velocities of the segments and the main body. The upper and lower rows correspond to the power and recovery strokes, respectively (note the use of different time steps). (b) The instanteous velocity in the axial direction (normalized by the arm length L) of the main body segment. The dashed red line indicates the mean velocity in the steady-state.

The effect of the various parameters of (3) has been investigated by a series of simulation runs, where the sculling amplitude A, the sculling offset ψ and the velocity ω are varied in the ranges of $5° \le A \le 25°$, $10° \le \psi \le 25°$, and $40°/\text{s} \le \omega \le 75°/\text{s}$, respectively. (Note that the span for ω has been selected to be in accordance with the CFD studies presented in Section IV). The results, with regard to the mean velocity V attained by the system in the steady-state, are shown in the plots of Fig. 10. More specifically, Fig. 10a shows that, for the investigated range of parameters, the sculling amplitude A has a very limited effect on the mean

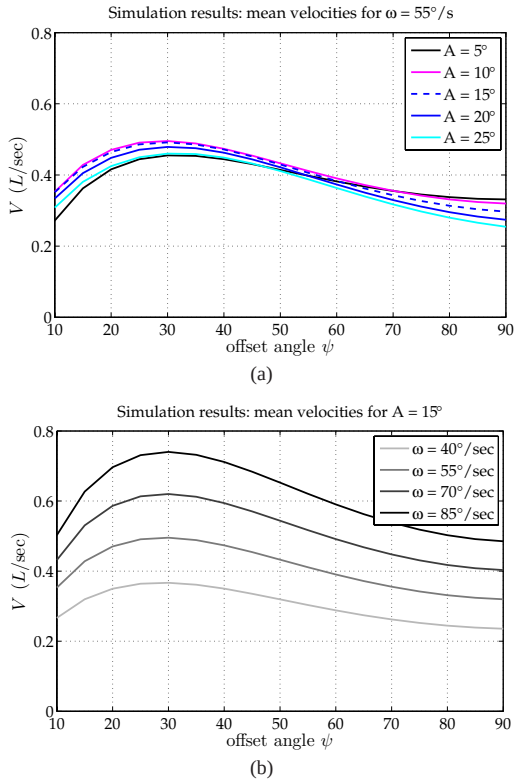

Fig. 10. Simulation results for the mean steady-state velocity (normalized by the arm length L) attained by the system over a range of values for the sculling amplitude A, the sculling offset ψ, and the angular velocity ω.

velocity. Although perhaps counter-intuitive, this observation should be weighted against the fact that, in these studies, an increase in A results in a longer overall period of the sculling motion (since ω is held constant). On the other hand, the results indicate considerable dependence of the velocity on the sculling offset, for which V can be seen to attain its maximum values for $\psi \simeq 30°$. In addition, the mean attained velocity increases with the overall frequency of the sculling arm movements (Fig. 10b).

B. Combining Sculling with Arm Undulations

We have also investigated a swimming mode where sculling movements are combined with arm undulations, so that a travelling wave is propagated along the arms, towards their tips. This could be seen as a first attempt to better approximate the complex kinematics of the octopus' multi-arm swimming, since sculling only captures the fast power stroke/slow recovery stroke aspect.

The travelling wave is implemented by prescribing sinusoidal oscillations for the joint angles of the arm segments [18], [19], according to:

$$\phi_i(t) = B_i \sin\left(\frac{2\pi}{T_u}t + (i-2)k\frac{2\pi}{N} + \chi\right) \ , \ i = 2...N, \tag{4}$$

where B_i is the oscillation amplitude of the ith segment, T_u is the oscillation period, and k represents the number of wavelengths propagating on the arm. Finally, χ is a phase shift, used to adjust the relative timing between the undulation and the sculling. Evidently, there are many different schemes possible for prescribing the shape of the travelling wave, as well as combining the undulations with the sculling motion. In the present study, we have restricted our investigations to travelling waves characterized by a common oscillation amplitude B for all the segments, and we have specified the period of the segments' oscillation to equal the overall period of the sculling motion, by setting $T_u = T_s$. Moreover, the case has been considered where the two arms perform these combined movements in anti-phase, thus ensuring the cancellation of sideforces.

Selected results from a parametric study, performed with $A = 5°$, $\psi = 20°$, are shown in Fig. 11, and suggest that, for appropriate parameter choices, the combination of undulations with sculling can yield significant performance enhancements, in terms of the attained mean swimming speed (c.f. Fig. 10). Snapshots from a simulation run of the combined mode are shown in Fig. 12

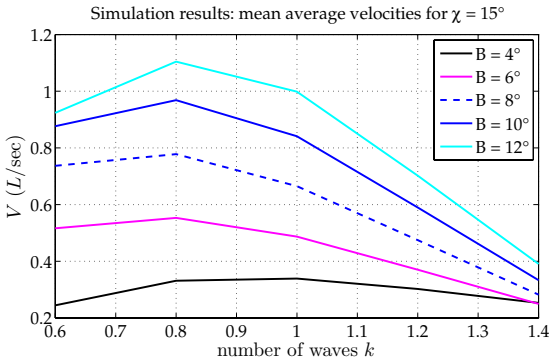

Fig. 11. Simulation results for the mode combining sculling with undulations: Mean velocities attained in the steady-state for a varying number of wavelengths propagating along the arms, and for different oscillation amplitudes.

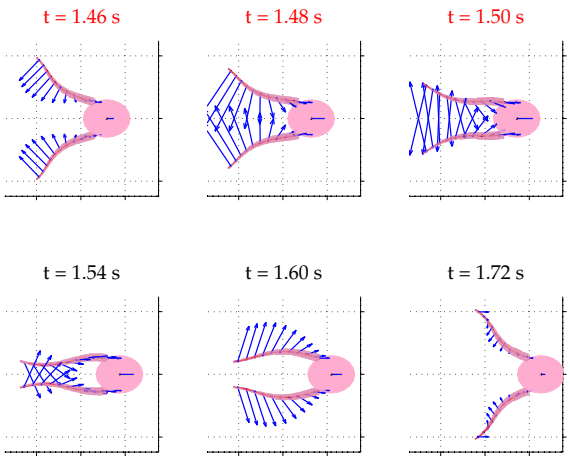

Fig. 12. Visualization of the mechanism for one period of sculling combined with undulations. Blue arrows denote velocities, while the upper and lower rows correspond to the power and recovery strokes, respectively (note the use of different time steps). Parameters were $A = 5°$, $\psi = 20°$, $\omega = 40°/s$, $B = 10°$, $k = 0.8$, and $\chi = 20°$.

Preprint submitted to 2012 IEEE International Conference on Robotics and Automation. Received September 16, 2011.

VI. EXPERIMENTS

Two octopus arms, with suckers of the same configuration and aspect ratios as those of the straight arm in Fig. 3a-I, in mirrored arrangement, were fabricated using a 3D printer (Elite, Dimension, USA) and were tested in a water tank, for a range of sculling movements, similar to the above simulations.

The experimental setup (Fig. 13) consisted of a water tank, the two-arm mechanism and a high accuracy digital force sensor (FMI220, Alluris GmbH, Germany: sampling frequency 1kHz, accuracy 1mN). The water tank was made from 5 mm thickness Plexiglas (interior dimensions are, length: 40 cm, width: 50 cm, height: 50 cm), and was filled with tap water at room temperature. The two arms, which had an overall length of $200\,\mathrm{mm}$ and a base diameter of $20\,\mathrm{mm}$, were positioned horizontally in water and were able to counter-rotate at the same rotational speed with the help of a servomotor (HS-65MG, Hitech, USA) and a gearbox. The mechanism was suspended, via an aluminum rod, from a platform mounted on the top of the tank. At a vertical distance of $290\,\mathrm{mm}$ above the system, the force sensor was positioned to record the axial component of the force applied to the rod from the arms movements. The distance between the centers of rotation of the two arms was $25\,\mathrm{mm}$.

For the preliminary tests presented here, the arms performed sculling movements with 10° and 20° amplitude, around various offsets in the 20° to 35° range, with angular velocities of 1 rad/s and 6 rad/s for the recovery and the power strokes, respectively. The results, shown in Fig. 14, confirm that the arms' sculling motions generate forces whose mean values are in the forward direction. Furthermore, the results indicate that the maximum of the mean recorded forces occurs, for both amplitudes, at the 30° offset angle, while the increase of the amplitude appears to have a very small effect on this maximum velocity. These observations are consistent with the mean velocity results from the simulations (c.f. Fig. 10a), providing evidence in support of our previous analysis.

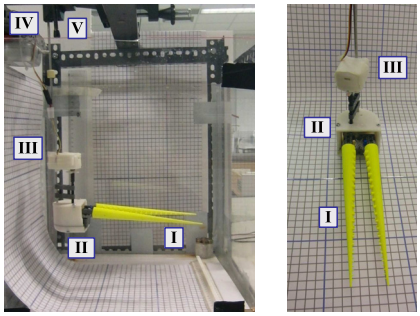

(a) (b)

Fig. 13. Experimental setup of the two-arm robotic prototype used for testing sculling movements. (I) arms, (II) gearbox housing, (III) servomotor housing, (IV) force sensor, (V) mounted platform.

VII. DISCUSSION AND CONCLUSIONS

Aquatic propulsion, inspired by the octopus arm swimming behavior, was studied via a two-arm multi-segmented computational model. CFD studies indicate the complexity of the flow structure around such arm configurations and the need for a closer investigation of the generated hydrodynamic loads. A methodology has been introduced for employing the results of the CFD analysis to assess the validity of the fluid drag model, commonly used in the robotics literature, and to specify the associated coefficients. In the present study, mean values for the normalized normal and tangential force coefficients were extracted from CFD data for various configurations of rotating arms, for each individual segment. The coefficients were then imported into the SIMUUN simulation tools. The latter were used to develop models for investigating preliminary approximations of locomotion modes capturing basic aspects of octopus-like multi-arm swimming. In particular, the proposed sculling mode implements the basic two-stroke mechanism, the efficacy of which can be further enhanced when appropriately combined with undulations. Preliminary experimental results, with the use of a robotic prototype, correlate well with the findings of the simulations.

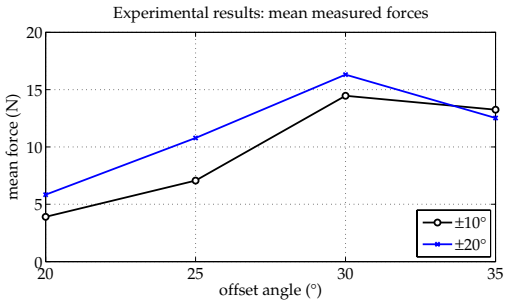

Fig. 14. Mean forces produced by the sculling movement of the robotic two-arm prototype, rotating $\pm 10^o$ and $\pm 20^o$ around various offsets.

Additional parametric studies, both computational and experimental, are expected to provide further insights regarding the propulsion and gait generation characteristics of these modes. Moreover, extensions of these modes to 8-arm models will be developed. Future work will also involve CFD studies of sculling movements and flexible arms to further assess whether the fluid drag model adequately captures the hydrodynamic effects of these complex movements. The findings of these investigations could be used towards the development of novel robotic underwater manipulators with multi-function capabilities.

VIII. ACKNOWLEDGMENTS

The authors would like to thank Prof. B. Hochner for his valuable input on octopus arm swimming, and Dr. V. Vavourakis and Mr. J. Oikonomidis for their help with the simulation studies.

REFERENCES

[1] C. Huffard, "Locomotion by abdopus aculeatus (cephalopoda: Octopodidae): Walking the line between primary and secondary defenses," *J. Exp. Biol.*, vol. 209, pp. 3697– 3707, 2006.

[2] G. Sumbre, Y. Gutfreund, G. Fiorito, T. Flash, and B. Hochner, "Control of octopus arm extension by a peripheral motor program," *Science*, vol. 293, pp. 1845–1848, 2001.

[3] C. Laschi, B. Mazzolai, V. Mattoli, M. Cianchetti, and P. Dario, "Design of a biomimetic robotic octopus arm," *Bioinspir. Biomim.*, vol. 4, no. 1, pp. 015 006–1–8, 2009.

[4] M. Cianchetti, V. Mattoli, B. Mazzolai, and P. D. C. Laschi, "A new design methodology of electrostrictive actuators for bio-inspired robotics," *Sensors and Actuators B: Chemical*, vol. 142, no. 1, pp. 288–297, 2009.
[5] R. Kang, A. Kazakidi, E. Guglielmino, D. Branson, D. Tsakiris, J. Ekaterinaris, and D. Caldwell, "Dynamic model of a hyper-redundant, octopus-like manipulator for underwater applications," in *Proc. IEEE/RSJ Int. Conf. on Intelligent Robots and Systems (IROS'11)*, 2011.
[6] G. Taylor, "Analysis of the swimming of long and narrow animals," *Proc. Roy. Soc. A*, vol. 214, pp. 158–183, 1952.
[7] Ö. Ekeberg, "A combined neuronal and mechanical model of fish swimming," *Biol. Cybern.*, vol. 69, no. 5-6, pp. 363–374, 1993.
[8] A. Ijspeert, "A connectionist central pattern generator for the aquatic and terrestrial gaits of a simulated salamander," *Biol. Cybern.*, vol. 85, no. 5, pp. 331–348, 2001.
[9] K. A. McIsaac and J. P. Ostrowski, "Experimental verification of open-loop control for an underwater eel-like robot," *Int. J. Rob. Res.*, vol. 21, pp. 849–860, 2002.
[10] M. Epstein, J. E. Colgate, and M. A. MacIver, "A biologically inspired robotic ribbon fin," in *Proc. IEEE/RSJ Int. Conf. on Intelligent Robots and Systems (IROS'05)*, 2005, (workshop on Morphology, Control, and Passive Dynamics).
[11] Y. Yekutieli, R. Sagiv-Zohar, R. Aharonov, Y. Engel, B. Hochner, and T. Flash, "Dynamic model of the octopus arm. i. biomechanics of the octopus reaching movement," *J. Neurophysiol.*, vol. 94, no. 2, pp. 1443–1458, 2005.
[12] F. Grasso, "Octopus sucker-arm coordination in grasping and manipulation," *Amer. Malac. Bull.*, vol. 24, no. 1, pp. 13–23, 2008.
[13] J. E. A. Kazakidi, V. Vavourakis and D. Tsakiris., "Computational investigationof octopus arm hydrodynamics," in *4th ANSA & ETA International Conference, Thessaloniki, Greece*, 2011.
[14] D. Tritton, *Physical Fluid Dynamics*. Oxford University Press, 1988.
[15] G. Batchelor, *An Introduction to Fluid Dynamics*. Cambridge University Press, 2000.
[16] Y. Gutfreund, T. Flash, Y. Yarom, G. Fiorito, I. Segev, and B. Hochner, "Organization of octopus arm movements: A model system for studying the control of flexible arms," *J. Neurosc.*, vol. 16, pp. 7297–7307, 1996.
[17] Y. Yekutieli, R. Mitelman, B. Hochner, and T. Flash, "Analyzing octopus movements using three-dimensional reconstruction," *J. Neurophysiol.*, vol. 98, pp. 1775–1790, 2007.
[18] M. Sfakiotakis and D. P. Tsakiris, "Undulatory and pedundulatory robotic locomotion via direct and retrograde body waves," in *Proc. IEEE/RSJ Int. Conf. on Robotics and Automation (ICRA'09)*, may 2009, pp. 3457 –3463.
[19] M. Sfakiotakis and D. Tsakiris, "Biomimetic centering for undulatory robots," *Intl. J. Rob. Res.*, vol. 26, no. 11/12, pp. 1267–1282, 2007.